ADVANCED MATERIALS INTERFACES
www.advmatinterfaces.de

Titanium Dioxide/Lithium Phosphate Nanocomposite Derived from Atomic Layer Deposition as a High-Performance Anode for Lithium Ion Batteries

Biqiong Wang, Jian Liu, Qian Sun, Biwei Xiao, Ruying Li, Tsun-Kong Sham, and Xueliang Sun**

Atomic layer deposition (ALD) is considered as a powerful technique to synthesize novel electrode materials for lithium-ion batteries (LIBs), because not only the compositions can be specifically designed to achieve higher battery performances, but also the materials can be deposited on various substrates for different purposes. Herein, a novel design of active material/electrolyte mixture electrode, i.e., titanium dioxide/lithium phosphate (TLPO) nanocomposite, has been successfully developed by ALD and deposited on carbon nanotube substrates (CNTs@TLPO) at 250 °C, by combining the ALD recipes of TiO_2 and lithium phosphate (LPO). In the nanocomposite, TiO_2 forms anatase nanocrystals, embedded in a matrix of amorphous lithium phosphate. CNTs@TLPO has been examined as an anode material for LIBs, exhibiting a similar electrochemical response as anatase TiO_2 in the cyclic voltammetry testing. CNTs@TLPO presents an outstanding capacity of 204 mA h g^{-1} upon 200 cycles in charge and discharge cycling measurements, as well as a significantly improved rate capability compared with ALD deposited TiO_2 on CNTs without LPO ALD cycles. This work shows that the in situ addition of solid-state electrolyte (e.g., lithium phosphate), which introduces higher Li^+ ionic conductivity, is an efficient way to achieve high-performance electrode materials for LIBs by ALD.

1. Introduction

In recent years, lithium-ion batteries (LIBs) have been aggressively pursued for portable electronic devices. In order to reduce the dependence on fossil fuels at present, there has been a drastic expansion of the market of electric vehicles (EVs) and hybrid electric vehicles (HEVs), for whose applications LIBs are considered the most promising storage system due to their high energy density and long cycle life. Intensive studies have been focused on improving LIBs in the aspects of power and energy density, cycling lifetime, safety characteristics, and cost, in order to fulfill the ever-increasing demand of EVs and HEVs.[1,2] However, the state-of-the-art LIBs are still insufficient enough to meet the strict standard of future EVs in terms of power output and driving distance. It is expected that the desired improvements on LIBs can be achieved by engineering novel architectures on current electrode materials and developing all-solid-state batteries.

TiO_2 has been studied extensively as an anode material for LIBs, since it is stable, environmentally benign, and of low fabrication cost. It also delivers a high Li-insertion potential (≈1.7 V versus Li/Li^+) and has a rather low self-discharge rate.[3–6] Considering electrochemical performance of different polymorphs of TiO_2, anatase TiO_2 is remarkable of its reversible uptake of 0.5 Li per formula unit, leading to a theoretical charge storage capacity of 167.5 mA h g^{-1}.[3,4] However, TiO_2 suffers from poor electronic conductivity and slow lithium-ion diffusion kinetics. The Li^+ ion diffusion coefficient in anatase TiO_2 is ≈10^{-13}–10^{-17} cm^2 s^{-1}. The electronic conductivity of anatase is also low at ≈10^{-12} S cm^{-1}.[7] The problems can be addressed from two perspectives. First, TiO_2 can be combined with highly conductive materials, such as carbon nanotubes (CNTs) and graphene.[8–10] To further boost the electrochemical performance, a Li^+ ion conductive material can be applied to help facilitate ion transport. Li et al. reported improved battery performance by coating the electrode material with solid-state electrolyte.[11] The second approach to solving the problems is nanostructuring. The downsizing dimensions not only significantly reduce the ionic and electronic diffusion length but also provide a high surface area, giving high rate and cycling performances.[12]

Atomic layer deposition (ALD) is a gas-phase deposition technique and capable to uniformly deposit ultrathin TiO_2 on materials of high aspect ratios. ALD is featured by two sequentially cyclic self-limiting reactions. The saturated surface reactions allow the film to grow layer-by-layer,

B. Wang, Dr. J. Liu, Dr. Q. Sun, B. Xiao, R. Li, Prof. X. Sun
Department of Mechanical and Materials Engineering
University of Western Ontario
London, ON N6A 5B9, Canada
E-mail: xsun9@uwo.ca
B. Wang, Prof. T.-K. Sham
Department of Chemistry
University of Western Ontario
ON N6A 5B7, Canada
E-mail: tsham@uwo.ca

DOI: 10.1002/admi.201600369

ADVANCED MATERIALS INTERFACES
www.advmatinterfaces.de

Materials Views
www.MaterialsViews.com

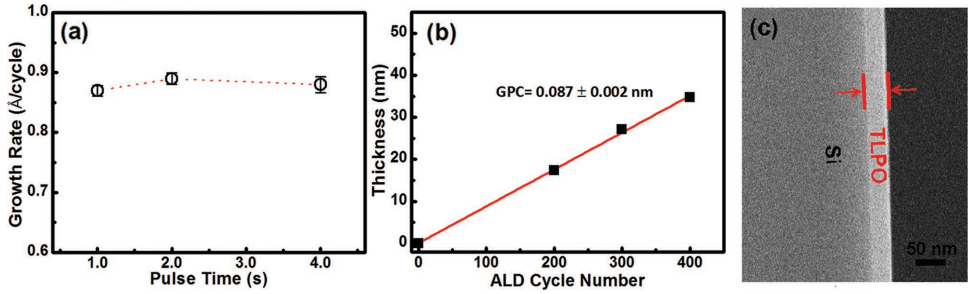

Figure 1. a) Growth per cycle (GPC) of TLPO thin films as a function of TTIP pulse time. b) Film thickness of TLPO as a function of ALD cycle number on a Si (100) substrate with a TTIP pulse time of 1 s at 250 °C. c) SEM image of cross-section of 400 ALD cycles of LTPO thin film deposited on the Si substrate.

providing extremely precise control of thickness at atom level.[13] Owing to these advantages, many research groups have demonstrated that ALD can be employed for direct synthesis of nanosized electrode materials for LIBs, including metal oxides, sulfides, and lithium containing materials (like $LiCoO_2$ and $LiFePO_4$).[14–19]

Meanwhile, the deposition of TiO_2 by ALD has been well established.[20,21] $TiCl_4$ and titanium tetraisopropoxide (TTIP, $Ti(OCH(CH_3)_2)_4$) are two most common titanium sources, with water as the most widely used oxidizer. Compared with $TiCl_4$, the usage of TTIP avoids the generation of corrosive HCl byproduct or chlorine containing residues in the thin film deposited.[21] Previous studies have shown that the structural phase of TiO_2 can be tuned by changing the deposition temperature. Amorphous TiO_2 can be achieved at lower temperatures (≈150 °C) while anatase phase is obtained at higher temperatures (≈250 °C).[13,21] The application of ALD TiO_2 involves the deposition on different substrates like Ni, Au, and Si to fabricate 3D batteries.[22–27] Also, amorphous TiO_2 by ALD has been deposited on nanocarbon materials (CNTs and graphene) as an anode in LIBs.[7,28]

Recently, a new strategy to mix electrolyte into electrode materials has been proposed, in order to increase the ionic conductivity of the overall electrode and improve the performance of all-solid-state batteries.[29–33] Actually, ALD technique has been also recently applied to fabricate various solid-state electrolytes.[34–40] The ALD process of amorphous lithium phosphate (LPO) was reported, using lithium tert-butoxide [LiO^tBu, $(CH_3)_3COLi$] and trimethylphosphate [TMPO, $(MeO)_3PO$] to react directly without water.[37] LPO was proved to be a promising candidate as a solid-state electrolyte with good ionic (Li^+) conductivity.[38] However, there has been still no report on in situ building a mixed active electrode material/electrolyte with a single combined ALD process. Thus, we herein choose anode material TiO_2 and solid-state electrolyte LPO to verify the feasibility of this strategy in ALD electrodes for LIBs.

In this work, we developed a novel nanocomposite of anatase TiO_2/lithium phosphate (TLPO) on CNTs (denoted as CNTs@TLPO) by ALD. The ALD processes of TiO_2 and LPO were applied in sequence at 250 °C to create a continuous matrix of the nanocomposite. TLPO thin film was uniformly and conformally deposited on CNTs. The electrochemical performances of CNTs@TLPO as anode in LIBs was also compared with ALD-deposited anatase TiO_2 on CNTs (designated as CNTs@T).

2. Results and Discussion

The ALD growth features of TLPO thin films were first characterized on standard Si (100) substrates. One ALD cycle consisted of two subcycles of TiO_2 and one of LPO in order to achieve higher ratio of TiO_2 as the active anode material. Keeping this ratio of subcycles, the effect of pulse time of TTIP on the growth rate of TLPO thin films at 250 °C is shown in **Figure 1**a, with the pulse time of water kept at 0.5 s. The growth per cycle (GPC) of TLPO thin films remained constant while the pulse time of TTIP increased, indicating that a saturated growth was obtained. Thus, a pulse time of 1 s TTIP with 0.5 s H_2O was used in the subsequent experiments. Moreover, a linear relation between the film thickness and the ALD cycle number has been observed at 250 °C, yielding a GPC of 0.087 nm in Figure 1b. The self-limiting characteristics of TiO_2 and LPO subcycles were responsible for the linear cycle dependence. If simply assuming the GPC of LPO subcycle is ≈0.057 nm per cycle, same as our previous result for ALD LPO thin film growth,[38] the growth rate of TiO_2 at 250 °C could be estimated as 0.015 nm per cycle, which is relatively lower than the value (≈0.024 nm per cycle) reported in previous study.[13] This could be due to the difference in the surface chemistry between the preceding and the succeeding subcycles, leading to a deviated GPC of one or each binary system in the combined ALD process.[34,36] In this case, it is reasonable to lower GPC of TLPO thin films than the linear combination of the GPC of TiO_2 and LPO. Besides, this result may also imply a strong interaction between the TiO_2 and LPO phases in the ALD TLPO thin films, which is expected to contribute a better ion transportation and exchange behavior in the electrode. Scanning electron microscope (SEM) image of a cross-section of TLPO thin film after 400 ALD cycles on Si substrate is displayed in Figure 1c. It can be seen that TLPO thin film is uniformly deposited on the Si substrate, giving a flat surface on the substrate, with a thickness of about 35 nm.

The chemical states of the light elements in TLPO thin films were determined by X-ray photoelectron spectroscopy (XPS) using synchrotron radiation. The photon energies used for Li 1s and P 2p spectra were 160 and 210 eV, respectively. Due to the much lower energy of the excitation photons (often higher cross-section) and higher energy resolution than laboratory X-rays, soft X-ray photoelectron spectroscopy using synchrotron radiation is more sensitive to the variation of electronic states at the surface and enables us to study the core-level of lithium

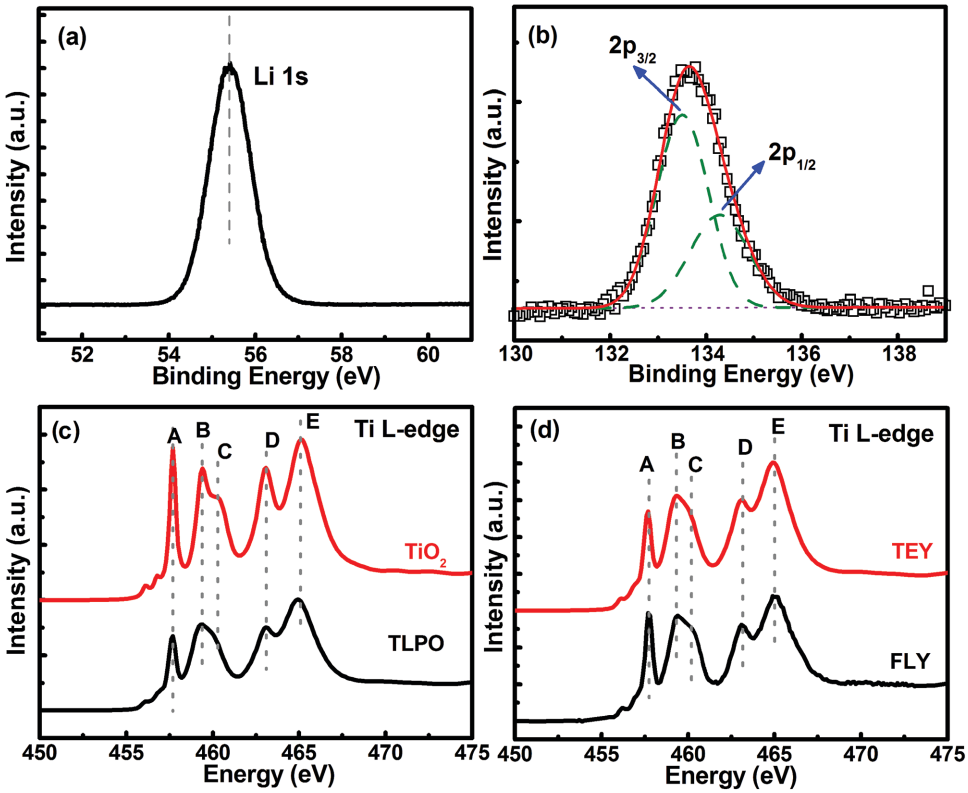

Figure 2. Photoelectron spectra of TLPO thin films deposited on the Si substrate: a) Li 1s (the photon energy is 160 eV); b) deconvolution of P $2p_{3/2,1/2}$ (with a photon energy of 210 eV); Ti $L_{3,2}$-edge XANES spectra: c) TEY spectra of ALD deposited TLPO and TiO_2 thin films; d) TEY and FLY spectra of TLPO as-deposited.

in greater details.[41] The Li 1s and P 2p XPS spectra of TLPO are presented in **Figure 2**. It is obvious that the Li 1s spectrum contains only one symmetric peak as shown in Figure 2a, suggesting that Li is in the single chemical environment of Li (Li-O) in the TLPO thin film. The peak position locates at 55.35 eV, which is in accordance with our previous work of ALD LPO.[42,43] The P 2p spectrum in Figure 2b can be fitted into a set of doublet, P $2p_{1/2}$ and $2p_{3/2}$, which are centered at 134.21 and 133.42 eV, respectively,[42–44] corresponding to the phosphorous in phosphate. This result is consistent with the spectrum of Li 1s. The XPS results confirmed the successful deposition of LPO in the nanocomposite TLPO. In addition, the LPO component in the TLPO thin films shared the same chemical states with the lithium phosphate thin films deposited by ALD at the same temperature (250 °C).[38]

X-ray absorption spectroscopy (XAS) was employed to study the local chemical environment of Ti by exciting the core electron to the previously unoccupied electronic states. Ti $L_{3,2}$-edge probes electron transition from Ti 2p to the conduction band of Ti 3d character (dipole selection rules). Spectra shown in Figure 2c were recorded in total electron yield (TEY) mode, which measures the total yield of photoelectrons, Auger electrons, and secondary electrons (dominant) upon X-ray excitation, revealing the information from the sample surfaces of a few nanometers.[45] A few characteristic features are observed and marked by vertical lines (Figure 2c). Peaks A, B, and C belong to the $2p_{3/2}$ to 3d transition (L_3-edge), while peaks D and E at a higher energy of a similar profile yet broadened, arise from the $2p_{1/2}$ to 3d transition (L_2-edge). At both edges, the crystal field splits the 3d band into t_{2g} (peaks A and D) and e_g (peaks B, C, and E) sub-bands. The e_g peak splitting (peaks B and C) results from the difference in local symmetry of the corresponding crystal phases.[46] The upper line represents the spectrum from ALD-deposited TiO_2 thin film at 250 °C and the lower one is from TLPO thin film. There is no evident energy shift between the onsets of edge jump the two spectra, suggesting that Ti in the two samples are of the same oxidation state (i.e., Ti^{4+}). The splitting of e_g band is well resolved in TiO_2 with peak B of a higher intensity than peak C, which is typical of anatase TiO_2. However, this feature is broadened in TLPO thin films, which can be associated with the loss of long-range order due to the effects of titanium interactions with second-neighboring atoms.[47] The addition of LPO component in the TLPO nanocomposite gives rise to the degradation of long-range order of TiO_2. Figure 2d compares the TEY and X-ray fluorescence yield (FLY) spectra of TLPO thin films. Differing from TEY, FLY measures the X-ray fluorescence emission which has two orders of magnitude increase in attenuation length in the solid than electrons, collecting bulk sensitive information.[45] The key features in FLY resemble those in TEY, which is indicative of a consistent and uniform distribution of Ti with the same chemical states in as-prepared TLPO thin films.

To determine the crystal structure of CNTs@TLPO, X-ray diffraction (XRD), transmission electron microscopy (TEM), and high resolution transmission electron microscopy (HRTEM)

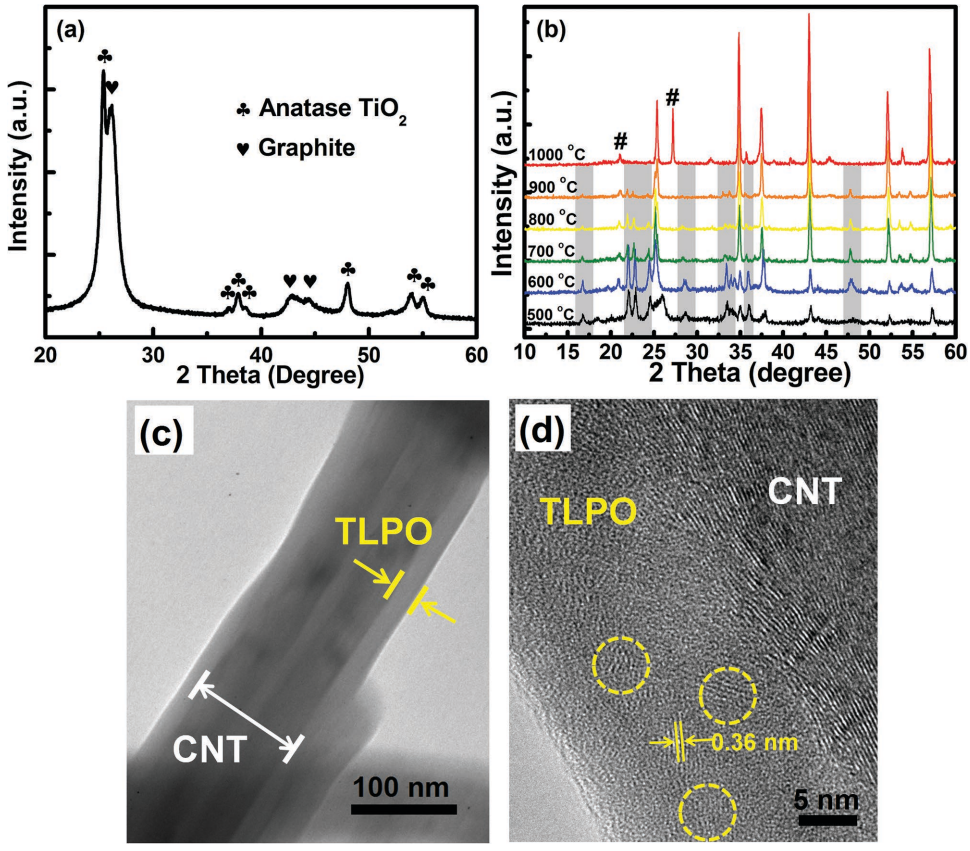

Figure 3. a) XRD spectrum of TLPO/CNTs. b) In situ XRD spectra of TLPO/CNTs. c) TEM image of CNTs@TLPO after 300 ALD cycles. d) HRTEM image of the CNTs@TLPO after 300 ALD cycles.

were employed and the results are shown in **Figure 3**. The diffraction peaks observed in Figure 3a located at 26°, 43°, and 44° (labeled with ♥), correspond to (002), (100), and (101) planes of graphic carbon (JCPDS No. 08-415) from CNTs. The rest peaks (labeled with ♣) are assigned to anatase TiO_2 (JCPDS No. 21-1272). The two sharp peaks located at 25° and 48° belong to the (101) and (200) planes of anatase TiO_2. It is known that XRD provides overall collective information of the powder samples. Therefore it can be concluded that the ALD grown TiO_2 crystallized in the anatase phase, which is consistent with previous reports.[13,47] In contrast, no diffraction peak of Li_3PO_4 was found in the XRD pattern, indicating that the LPO component in TLPO is amorphous. In order to further track the LPO phase, an in situ heating XRD measurement was carried out and the results are shown in Figure 3b. The peaks addressed to Li_3PO_4 (JCPDS No. 15-760) are highlighted, which were absent in the room temperature (RT) XRD spectrum and started to appear at 500 °C. Besides, the signals from the CNTs disappeared at elevated temperature (above 500 °C), caused by the combustion of carbon content during in situ heating in air. Both Li_3PO_4 and the anatase TiO_2 in the XRD patterns persisted till 1000 °C. Moreover, annealing from 500 to 800 °C resulted in better crystallinity of both components. No noticeable phase transformation was detected during the heat treatment. When the temperature reached 1000 °C, the patterns from either Li_3PO_4 or TiO_2 could not be discerned. The peaks were solely from the sample holders, which contained corundum Al_2O_3 (JCPDS No. 75-792) and quartz (JCPDS No. 79-1911, labeled with #). These in situ XRD results doubtlessly prove the existence of the amorphous Li—P—O phase in the as-grown TLPO thin films.

Microstructural information was provided by TEM and HRTEM as presented in Figure 3. The thickness of the as-prepared TLPO thin film on CNTs after 300 ALD cycles in Figure 3c were measured to be ≈23 nm, which was very close to the calculated result (≈26 nm) based on the GPC obtained on the Si substrate, indicating a similar ALD growing behavior on both substrates. The negligible deficiency could be explained by the high aspect ratio of CNTs. The amount of the precursors that diffused into the porous powder substrates could be a little less than that on the 2D flat surface (Si). The hollow structure of multiwalled CNTs is clearly revealed, with the surface evenly covered with TLPO thin films. Furthermore, the HRTEM image in Figure 3d discloses the detailed structure of the nanocomposite. Aligned lattices can be observed in the HRTEM image of CNT@TLPO, as some spots highlighted in the circled regions. The interplanar spacing of plane obtained from the pixel intensity profile of the selected regions is 0.36 nm, which matches the plane (101) of bulk anatase TiO_2.[8,48] Moreover, it is clearly shown that the nanocrystalline anatase TiO_2 randomly dispersed in the amorphous LPO matrix. It has been reported that ALD process at elevated temperatures resulted in anatase TiO_2.[13] The nucleation sites at the early stage of the ALD process, in this case, was highly possible to be affected by the roughness and the functional groups on the surface of the

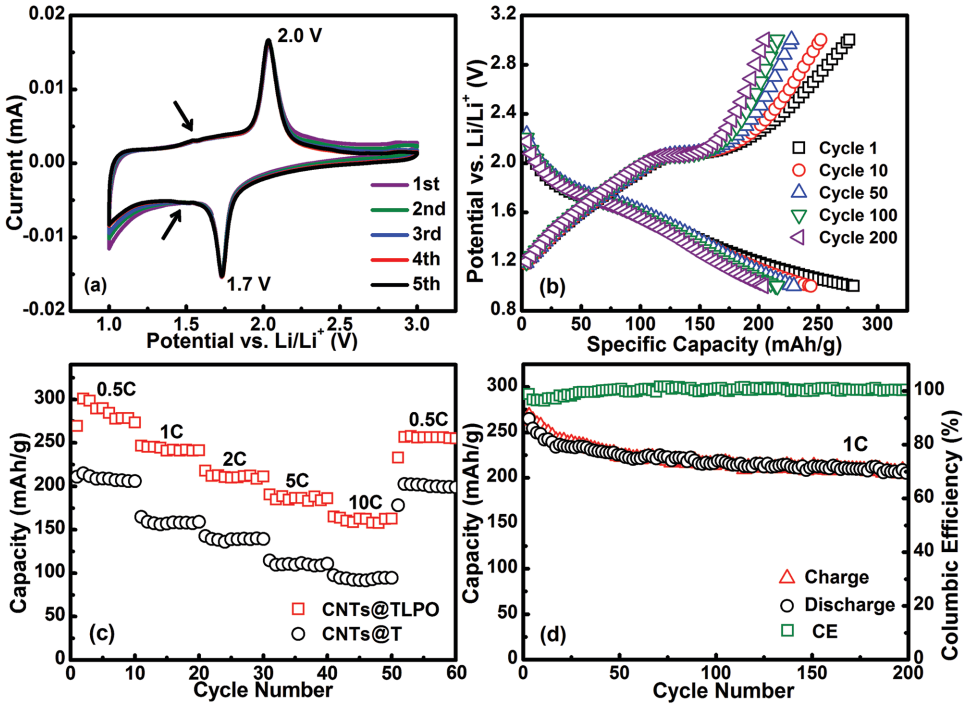

Figure 4. a) Cyclic voltammetry (CV) curves of TLPO/CNTs using a voltage window of 1.0–3.0 V versus Li/Li^+. b) Charge/discharge profiles of cycles 1, 50, 100, and 200 at a current density of 1C (160 mA g^{-1}) in a voltage window of 1.0–3.0 V. c) Rate capability of CNTs@TLPO at current density of 0.5, 1, 2, 5, and 10C. d) Cycling stability of CNTs@TLPO at a current density of 1C (1.0–3.0 V).

substrates (CNTs). Meanwhile, when the LPO ALD process was added, the continuous growth of TiO_2 was interrupted. Some available sites remained was taken by the growth of LPO component. Consequently when proceeding to the TiO_2 subcycle again, it tended to grow on favorable sites which most likely were some of the initial sites. Thus, after repeating this process, a nanocomposite with nanocrystal TiO_2 distributed in the amorphous LPO matrix was formed. To conclude the aforementioned discussions, TLPO nanocomposite was successfully synthesized via ALD by combining the subcycles of TiO_2 and lithium phosphate. The TLPO thin films could be evenly coated on CNTs. The as-prepared nanocomposite consisted of anatase TiO_2 nanocrystals wrapped in amorphous lithium phosphate matrix, as shown in the schematic diagram (Figure 5).

Thermogravimetric analysis (TGA) was performed to analyze the weight percentage of CNTs@TLPO and CNTs@T. The results can be found in Figure S1 (Supporting Information), yielding 45.2% and 67.1% loading of TLPO and TiO_2, respectively. The high mass loadings of the TLPO and TiO_2 are crucial to the successful implementation of ALD to deposit active materials on conductive substrates to fabricate electrodes for LIBs. Energy dispersive spectroscopy (EDS) results were also obtained to evaluate the content ratio of TiO_2 and LPO in the CNTs@TLPO sample (Figure S2, Supporting Information). Both signals from elements Ti and P were detected, giving an atomic ratio of 1.81, close to the subcycle number ratio of TiO_2 to LPO with reasonable of TiO_2 loading in the CNTs@TLPO nanocomposite.

Electrochemical measurements were then conducted on CNTs@TLPO and CNTs@T. **Figure 4**a displays cyclic voltammetry (CV) curves of CNTs@TLPO in the first five cycles. A pair of well-defined current peaks can be observed at 1.7 V (cathodic sweep) and 2.0 V (anodic sweep), which are the characteristic for the lithium-ion intercalation/deintercalation reaction in anatase TiO_2.[9] The voltage polarization between the two current peaks reflects the overpotential required for the transformation between TiO_2 and Li_xTiO_2 during lithiation/delithiation. A 0.3 V difference in the CV for CNTs@TLPO is slightly reduced than the reported value for nanocrystalline TiO_2 (0.4 V),[3,49] presaging an easier transition between the two phases, which may have been benefited from the core–shell electron conduction from CNT and ionic diffusion from LPO electrolyte phase. In addition, the redox current peaks exhibited nearly no decrease after five CV cycles. Meanwhile, the ratio of anodic and cathodic peak current was retained close to 1, indicating good reversibility and equilibrium redox system of CNTs@TLPO throughout the potential scan.[49] Interestingly, it can be observed that a pair of bumps appeared in the broad envelope region at lower potentials envelope at around 1.4/1.55 V. Similar phenomena have been reported before.[3,49–51] It was ascribed to the probable trace of another TiO_2 polymorph, which might cause extra contribution to capacity.[3,49–51] Turning to the charge–discharge voltage profiles, Figure 4b depicts the profiles of cycles 1, 10, 50, and 200 of CNTs@TLPO at the current rate of 1C (160 mA g^{-1}). The plateaus are laid around the potential of 1.7/2.0 V, which matched the positions of the redox peaks in CV. Also, the plateaus and shapes of the charge/discharge curves are well maintained even after 200 cycles of cycling, suggesting stable dynamics of the lithium insertion/extraction process.[8] The capacity for all the CNTs@TLPO and CNTs@T electrodes was calculated based on the loadings of TLPO and TiO_2 thin films, respectively. The initial discharge and charge

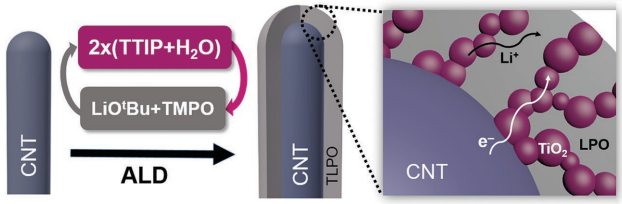

Figure 5. Schematic diagram of the fabrication process of CNTs@TLPO and the detailed structure of CNTs@TLPO.

capacities of CNTs@TLPO were 280.0 and 276.4 mA h g^{-1}, respectively. It should be noted that the applied voltage window was from 1 to 3 V, while the CNTs contributed negligible Li^+ storage in this voltage range (Figure S3, Supporting Information). Pure CNTs was also tested and it is confirmed that the specific capacity contribution from pure CNTs was negligible between 1 and 3 V (Figure S4, Supporting Information).[52]

To investigate the rate capability of CNTs@TLPO with CNTs@T as comparison, the electrodes were discharged and charged at various current rates, namely 0.5C, 1C, 2C, 5C, and 10C, shown in Figure 4c. Apparently, the capacity decreases with increasing current density (which is equivalent to power density when multiplied by the average discharge voltage). At the current rates of 0.5C, 1C, 2C, 5C, and 10C, CNTs@TLPO delivered a specific capacity of 273, 241, 211, 186, and 163 mA h g^{-1}, correspondingly, higher than many good works reported on anatase TiO_2 nanocomposites.[8,51,53] Moreover, the discharge/charge capacities resumed when the rate was reduced back to 0.5C. With respect to CNTs@T, CNTs@TLPO always demonstrated substantially improved specific capacity at all different current rate from 0.5C to 10C, which became even more distinguished at higher rate. For instance, at 10C, the specific capacity of TLPO reached 162.8 mA h g^{-1}, almost two times of that of CNTs@T. Both CNTs@TLPO and CNTs@T took advantage of the conductive carbon "skeleton" as substrates for faster electron transportation (as shown in **Figure 5**) and the reduced diffusion path due to the nanoscale size of the active materials. Thus, the enhanced lithium diffusion kinetics of CNTs@TLPO compared to CNTs@T could be ascribed to the existence of LPO in the nanocomposite. LPO has proven to be a good solid-state electrolyte, which can efficiently transport lithium ions in and out of the material.[38,54,55] Based on previous structural analysis, the TiO_2 nanocrystals were dispersed in a matrix of LPO, "immersed" in an ionic conductive material which could significantly increase the diffusion rate of Li^+, as shown in Figure 5. Electrochemical impedance spectroscopy of CNTs@TLPO and CNTs@T electrodes was presented in Figure S5 (Supporting Information). Both Nyquist plots consisted of a high-frequency semicircle and a linear Warburg region at lower frequency. The high-frequency region was associated with the charge-transfer resistance related to Li^+ interfacial transfer. The lower charge-transfer resistance of CNTs@TLPO indicated a smaller ionic resistance and enhanced kinetics for CNTs@TLPO. It was further confirmed that the incorporation of Li^+ conducting material (LPO) into the nanocomposite helped achieve better Li^+ transport kinetics. At last, a stability test was carried out, as seen in Figure 4d. With an initial discharge capacity of 280.0 and 276.4 mA h g^{-1}, CE of the first cycle was 101.3% while in the second cycle, the discharge capacity dropped to 265.0 mA h g^{-1} with a coulombic efficiency (CE) of 98.9%, indicating an irreversible capacity loss due to trapping of Li^+ inside the framework. Surprisingly, after the initial break-in cycles where CE decreases (typically three cycles), CE increased back during the first 50 cycles and was sustained at about 100% afterward. Former studies believed that in the break-in cycles, the irreversible Li insertion sites were gradually filled and trace water was gradually oxidized and consumed at higher potentials and that the residue lithium remaining in the TiO_2 enhanced the electric conductivity,[56] thus improving the CE and decreasing the irreversible capacity accordingly. Furthermore, the discharge capacity was still retained at 204 mA h g^{-1} after 200 cycles, higher than that of the ALD deposited CNTs@T (149 mA h g^{-1}, shown in Figure S6 (Supporting Information)) under the same testing conditions. It is worth discussing that the specific capacity was even larger than the theoretical value (168 mA h g^{-1}) of anatase TiO_2 at 1C. Two postulations are proposed here. First, the matrix of LPO might act as a lithium storage media during the test, yielding higher capacity. Second, it has been well acknowledged that during the intercalation of Li^+, TiO_2 becomes Li_xTiO_2, where x is usually found to be 0.5 for anatase TiO_2, where the conventional theoretic capacity is reached. However, x could be close to 1 for amorphous TiO_2 and for very small anatase particles.[8,26,50,51] Apart from the biphasic transition from tetragonal to orthorhombic $Li_{0.5}TiO_2$, further insertion of Li^+ could form cubic $LiTiO_2$ with a higher capacity. In CNTs@TLPO, the nanocrystallines of TiO_2 were found to be around 5 nm (from Figure 3d), which might give rise to the formation of Li_xTiO_2 with x over 0.5 and therefore delivering a higher capacity.

Overall, this study demonstrates that the incorporation of LPO solid-state electrolyte can significantly improve the performance of ALD TiO_2 electrodes. It can be expected that applying and optimizing various choices of ALD electrolytes for ALD electrode materials can become a promising method to achieve high performance electrodes in future.

3. Conclusion

In summary, titanium dioxide/lithium phosphate nanocomposites (TLPO) have been successfully deposited using the ALD technique by combination of TTIP-H_2O and LiO^{t}Bu-TMPO subcycles. The overall growth can be well controlled in terms of film thickness. The two components TiO_2 and LPO were identified correspondingly, applying various techniques including XPS, XAS, XRD, and HRTEM. LPO was determined to be amorphous while TiO_2 existed in the form of anatase nanocrystallines distributed in the LPO matrix. TLPO thin films were deposited on CNTs to be applied as anode materials for LIBs. Compared with ALD deposited TiO_2 single phase on CNTs as anodes, CNTs@TLPO exhibited exceptional rate capability especially at high current rates. The reason could be ascribed to the use of CNT substrates and the adding of ionic conductive LPO component, which help to achieve faster Li^+ diffusion kinetics. Furthermore, excellent cycling performance of CNTs@TLPO

was obtained with a specific capacity of over 200 mA h g^{-1}, which could be contributed to the compositions, nanosized structure, the high surface area of the nanocomposite. The material designed here can be employed to form high power and high capacity electrode materials. Further, this work demonstrates that ALD can be employed to design and develop high-performance electrode materials for battery applications. It also holds great potential in fabricating all-solid-state batteries in future.

4. Experimental Section

Deposition of TLPO by ALD: TLPO was deposited in a Savannah 100 ALD system (Ultratech/Cambridge Nanotech., USA) by using TTIP ($Ti(OCH(CH_3)_2)_4$) and water for TiO_2 subcycle and LiO^tBu [$(CH_3)_3COLi$] and TMPO [$(MeO)_3PO$] for LPO subcycle. Source temperatures for TTIP, LiO^tBu, and TMPO were 80, 180, and 75 °C, respectively, while H_2O was kept at RT. The deposition of the nanocomposite was carried out at 250 °C. The chosen temperature was in the overlapped temperature range of the ALD windows of TiO_2 and LPO to achieve ALD growth and prevented precursors from decomposing. Additionally, the manifold was heated to 180 °C to avoid condensation of precursors. Nitrogen was used as the carrier gas. One ALD cycle consisted of two subcycles of TiO_2 and LPO. The overall sequence was the following: 2 × [TTIP (*x* s pulse/10 s purge) – H_2O (0.5 s pulse/15 s purge)] + [LiO^tBu, (2 s pulse/15 s purge) – TMPO (2 s pulse/15 s purge)]. The recipe of LPO subcycle was directly taken from the previous work.[38] Different pulse times of TTIP (1, 2, and 4 s) were used to verify the ALD process. Si (100) wafers and CNT powders were used as substrates for the deposition of TLPO. Before the ALD process, Si wafers were cleaned by acetone, ethanol, and water in sequence, followed by drying with flowing air. CNT powders were refluxed in nitric acid (HNO_3, 70%) for 3 h at 120 °C to remove the residual catalyst from the growth of CNTs and functionalize the surface of CNT. The treated CNTs were dispersed in ethanol and washed in ultrasonic bath. Then the solution was casted on Al foil and loaded in the ALD chamber for deposition.

Physical Characterization of TLPO: The thickness, morphology, and compositions were determined by a field emission scanning electron microscope (Hitachi S4800). Soft X-ray photoelectron spectroscopy (with a photon energy of 160 eV for Li 1s XPS and 210 eV for P 2p XPS) and X-ray absorption near-edge structure (XANES) spectroscopy were conducted at Canadian Light Source (CLS) on variable line spacing plane grating monochromator and spherical grating monochromator beamlines, respectively, in order to study the chemical states of the nanocomposite. Structural information was characterized by TEM (Hitachi 7000), HRTEM (JEOL 2010 FEG), and XRD system (Bruker D8 Advance, Cu-Kα X-ray source). High-temperature in situ XRD measurements (scan step of 0.02° s^{-1}) were conducted on CNTs@TLPO in air to study the temperature dependence of the phase transformation. Spectra were collected from 400 to 900 °C with a diffraction angle of 10°–60°. At each temperature, the sample was annealed for 1 h before the measurement was taken in a period of 15 min.

Electrochemical Characterization of CNTs@TLPO: Electrochemical measurements were performed on CNTs@TLPO and CNTs@T. TLPO was deposited on CNTs using 300 ALD cycles of 2 × [TTIP (1 s pulse/10 s purge) – H_2O (0.5 s pulse/15 s purge)] + [LiO^tBu, (2 s pulse/15 s purge) – TMPO (2 s pulse/15 s purge)]. 600 ALD cycles of TiO_2 was selected to maintain the same total cycle number of TiO_2, using the recipe: [TTIP (1 s pulse/10 s purge) – H_2O (0.5 s pulse/15 s purge)]. The loadings of CNTs@TLPO and CNTs@T were evaluated by TGA (SDT Q600) from RT to 1000 °C in air at a heating rate of 10 °C min^{-1}. EDS was done to estimate the content ratio of TiO_2 and LPO. Electrochemical performances were tested in coin-type half cells, using lithium foils as the counter electrode. CNTs@TLPO and CNTs@T were scraped gently off the Al foil and mixed with acetylene black and polyvinylideneuoride with a weight ratio of 8:1:1 in *N*-methylpyrrolidinone solvent. The electrode was fabricated using a slurry casting method.[11] Pure CNTs was fabricated into electrode using the same method and tested for comparison. The electrolyte was composed of 1 M $LiPF_6$ salt dissolved in ethylene carbonate:diethyl carbonate:ethyl methyl carbonate of 1:1:1 volume ratio. The cells were assembled in a glove box (Vacuum Atmosphere Company) under a dry argon atmosphere (moisture and oxygen level less than 1 ppm). CV (1–3 V, 0.1 mV s^{-1}) and electrochemical impedance spectroscopy were measured on the versatile multichannel potentiostat 3/Z (VMP3). Charge–discharge characteristics at a constant current mode were tested at RT on Arbin BT-2000 battery tester, at different current rates (1C = 160 mA g^{-1}) in a voltage window of 1–3 V. The specific capacity was calculated by dividing the obtained capacity with the weight of TLPO and TiO_2 deposited in the composite.

Supporting Information

Supporting Information is available from the Wiley Online Library or from the author.

Acknowledgements

This work was supported by the Nature Sciences and Engineering Research Council of Canada (NSERC), the Canada Research Chair Program, the Canada Foundation for Innovation (CFI), the Ontario Research Fund, the Canada Light Source at the University of Saskatchewan, the Canadian Centre for Electron Microscopy at McMaster University, and the University of Western Ontario. Dr. Jian Liu is grateful for financial support from NSERC Postdoctoral Fellowships program. The Canadian Light Source was supported by CFI, NSERC, NRC, CHIR, and the University of Saskatchewan.

Received: May 2, 2016
Revised: June 24, 2016
Published online:

[1] M. Armand, J.-M. Tarascon, *Nature* **2008**, *451*, 652.
[2] J. B. Goodenough, Y. Kim, *Chem. Mater.* **2010**, *22*, 587.
[3] J. S. Chen, Y. L. Tan, C. M. Li, Y. L. Cheah, D. Luan, *J. Am. Chem. Soc.* **2010**, *132*, 6124.
[4] S. Kumar, S. Lee, W. Yoon, H. Shin, *J. Power Sources* **2014**, *249*, 59.
[5] Y. Tang, Y. Zhang, J. Deng, J. Wei, H. Le Tam, B. K. Chandran, Z. Dong, Z. Chen, X. Chen, *Adv. Mater.* **2014**, *26*, 6111.
[6] Y. Tang, Y. Zhang, J. Deng, D. Qi, W. R. Leow, J. Wei, S. Yin, Z. Dong, R. Yazami, Z. Chen, X. Chen, *Angew. Chem., Int. Ed.* **2014**, *53*, 13488.
[7] M. Xie, X. Sun, C. Zhou, A. S. Cavanagh, H. Sun, T. Hu, G. Wang, J. Lian, S. M. George, *J. Electrochem. Soc.* **2015**, *162*, 974.
[8] H. Liu, W. Li, D. Shen, D. Zhao, G. Wang, *J. Am. Chem. Soc.* **2015**, *137*, 13161.
[9] Y. Cheng, Z. Chen, H. Wu, M. Zhu, Y. Lu, *Adv. Funct. Mater.* **2016**, *26*, 1338.
[10] Y. Tang, Y. Zhang, X. Rui, D. Qi, Y. Luo, W. R. Leow, S. Chen, J. Guo, J. Wei, W. Li, J. Deng, Y. Lai, B. Ma, X. Chen, *Adv. Mater.* **2016**, *28*, 1567.
[11] X. Li, J. Liu, M. N. Banis, A. Lushington, R. Li, M. Cai, X. Sun, *Energy Environ. Sci.* **2014**, *7*, 768.
[12] S. K. Panda, Y. Yoon, H. Suk, W. Yoon, H. Shin, *J. Power Sources* **2012**, *204*, 162.

[13] X. Meng, D. Geng, J. Liu, R. Li, *Nanotechnology* **2011**, *22*, 165602.
[14] X. Li, X. Meng, J. Liu, D. Geng, Y. Zhang, M. N. Banis, Y. Li, J. Yang, R. Li, X. Sun, M. Cai, M. W. Verbrugge, *Adv. Funct. Mater.* **2012**, *22*, 1647.
[15] N. P. Dasgupta, X. Meng, J. W. Elam, A. B. F. Martinson, *Acc. Chem. Res.* **2015**, *48*, 341.
[16] M. E. Donders, W. M. Arnoldbik, H. C. M. Knoops, W. M. M. Kessels, P. H. L. Notten, *J. Electrochem. Soc.* **2013**, *160*, A3066.
[17] J. Liu, M. N. Banis, Q. Sun, A. Lushington, R. Li, *Adv. Mater.* **2014**, *26*, 6472.
[18] X. Meng, X.-Q. Yang, X. Sun, *Adv. Mater.* **2012**, *24*, 3589.
[19] J. Liu, X. Sun, *Nanotechnology* **2015**, *26*, 024001.
[20] Y. Zhang, C. Guerra-nun, I. Utke, J. Michler, M. D. Rossell, R. Erni, *J. Phys. Chem. C* **2015**, *119*, 3379.
[21] X. Meng, M. Norouzi, D. Geng, X. Li, Y. Zhang, R. Li, H. Abou-Rachid, X. Sun, *Appl. Surf. Sci.* **2013**, *266*, 132.
[22] W. Wang, M. Tian, A. Abdulagatov, S. M. George, Y. Lee, R. Yang, *Nano Lett.* **2012**, *12*, 655.
[23] J. Ye, A. C. Baumgaertel, Y. M. Wang, J. Biener, M. M. Biener, *ACS Nano* **2015**, *9*, 2194.
[24] E. Eustache, P. Tilmant, L. Morgenroth, P. Roussel, G. Patriarche, D. Troadec, N. Rolland, T. Brousse, C. Lethien, *Adv. Energy Mater.* **2014**, *4*, 1301612.
[25] S. K. Cheah, E. Perre, M. Rooth, M. Fondell, A. Hårsta, L. Nyholm, M. Boman, J. Lu, P. Simon, K. Edstro, *Nano Lett.* **2009**, *9*, 3230.
[26] E. M. Lotfabad, P. Kalisvaart, K. Cui, A. Kohandehghan, M. Kupsta, D. Mitlin, *Phys. Chem. Chem. Phys.* **2013**, *15*, 13646.
[27] S. Kim, T. H. Han, J. Kim, H. Gwon, H. Moon, S. Kang, S. O. Kim, K. Kang, *ACS Nano* **2009**, *3*, 1085.
[28] C. Ban, M. Xie, X. Sun, J. J. Travis, G. Wang, H. Sun, A. C. Dillon, J. Lian, S. M. George, *Nanotechnology* **2013**, *24*, 424002.
[29] G. Delaizir, V. Viallet, A. Aboulaich, R. Bouchet, L. Tortet, V. Seznec, M. Morcrette, J. M. Tarascon, P. Rozier, M. Dolle, *Adv. Funct. Mater.* **2012**, *22*, 2140.
[30] S. Kinoshita, K. Okuda, N. Machida, M. Naito, T. Sigematsu, *Solid State Ionics* **2014**, *256*, 97.
[31] M. Nagao, A. Hayashi, M. Tatsumisago, *Electrochim. Acta* **2011**, *56*, 6055.
[32] M. Nagao, A. Hayashi, M. Tatsumisago, T. Ichinose, T. Ozaki, Y. Togawa, S. Mori, *J. Power Sources* **2015**, *274*, 471.
[33] X. Chen, *Chem. Soc. Rev.* **2015**, *44*, 5926.
[34] T. Aaltonen, M. Alnes, O. Nilsen, L. Costelle, H. Fjellvåg, *J. Mater. Chem.* **2010**, *20*, 2877.
[35] Y.-C. Perng, J. Cho, D. Membereno, N. Cirigliano, B. Dunn, J. P. Chang, *J. Mater. Chem. A* **2014**, *2*, 9566.
[36] J. Liu, M. N. Banis, X. Li, A. Lushington, M. Cai, R. Li, T.-K. Sham, X. Sun, *J. Phys. Chem. C* **2013**, *117*, 20260.
[37] J. Hamalainen, J. Holopainen, F. Munnik, T. Hatanpaa, M. Heikkila, M. Ritala, M. Leskela, *J. Electrochem. Soc.* **2012**, *159*, A259.
[38] B. Wang, J. Liu, Q. Sun, R. Li, T. Sham, *Nanotechnology* **2014**, *25*, 504007.
[39] M. Cui, P. S. Lee, *Chem. Mater.* **2016**, *28*, 2934.
[40] Y. Cao, X. Meng, J. W. Elam, *ChemElectroChem* **2016**, *210093*, 1.
[41] S. Tanaka, M. Taniguchi, H. Tanigawa, *J. Nucl. Mater.* **2000**, *287*, 1405.
[42] Y. W. Hu, I. D. Raistrick, R. A. Huggins, *J. Electrochem. Soc.* **1997**, *124*, 1240.
[43] A. T. Appapillai, A. N. Mansour, J. Cho, Y. Shao-horn, *Chem. Mater.* **2007**, *89*, 5748.
[44] Z. Jinli, W. Jiao, L. Yuanyuan, N. Ning, G. Junjie, Y. Feng, L. Wei, *J. Mater. Chem. A* **2015**, *3*, 2043.
[45] L. Liu, J. Chan, T. Sham, *J. Phys. Chem. C* **2010**, *114*, 21353.
[46] L. Liu, J. Li, T. Sham, *Can. J. Chem.* **2015**, *112*, 106.
[47] J. Liu, M. N. Banis, B. Xiao, Q. Sun, A. Lushington, R. Li, J. Guo, T. Sham, X. Sun, *J. Mater. Chem. A* **2015**, *3*, 24281.
[48] W.-Q. Wu, H.-S. Rao, Y. Xu, Y.-F. Wang, C.-Y. Su, D.-B. Kuang, *Sci. Rep.* **2013**, *3*, 1892.
[49] J. Wang, Y. Zhou, Y. Hu, R. O. Hayre, Z. Shao, *J. Phys. Chem. C* **2011**, *115*, 2529.
[50] L. Kavan, M. Kalba, I. Exnar, V. Lorenzen, R. Nesper, M. Graetzel, J. Heyrovsky, *Chem. Mater.* **2004**, *16*, 477.
[51] N. Li, G. Liu, C. Zhen, F. Li, L. Zhang, H. Cheng, *Adv. Funct. Mater.* **2011**, *21*, 1717.
[52] B. Xiao, X. Li, X. Li, B. Wang, C. Langford, R. Li, X. Sun, *J. Phys. Chem. C* **2014**, *118*, 881.
[53] D. Wang, D. Choi, J. Li, Z. Yang, Z. Nie, R. Kou, D. Hu, C. Wang, L. V. Saraf, J. Zhang, I. A. Aksay, J. Liu, *ACS Nano* **2009**, *3*, 907.
[54] J. B. Bates, N. J. Dudney, G. R. Gruzalski, R. A. Zuhr, A. Choudhury, *J. Power Sources* **1993**, *44*, 103.
[55] B. Wang, B. C. Chakoumakos, B. C. Sales, B. S. Kwak, J. B. Bates, *J. Solid State Chem.* **1995**, *115*, 313.
[56] B. A. R. Armstrong, G. Armstrong, J. Canales, R. García, P. G. Bruce, *Adv. Mater.* **2005**, *17*, 2003.